Multiplicative Road Models with Bounded Realizations Applied in Non-Linear Vehicle Road Dynamics

Walter V. Wedig*
*KIT-Karlsruher Institut für Technologie, Karlsruhe, Germany

Summary. Multiplicative road models generate stationary vehicle excitations which are distributed similar to Gaussian processes but bounded in any given range by means of suitable nonlinearities. For increasing multiplicative noise, the nonlinear process becomes uniformly distributed and change to sinusoidal distributions for growing noise intensities. Both, the multiplicative and sinusoidal roads, are applied to excite quarter car models with one degree of freedom in order to work out the dynamical behavior and stability of vehicle road systems and to discuss them in comparison with classical ground excitations by means of Gaussian models or harmonic wave roads.

1. Introduction to vehicle road dynamics

To introduce basics of vehicle road dynamics, Figure 1 shows the model of a quarter vehicle model [1-6] rolling with constant speed v on a wavy road with level z and frequency $\Omega > 0$ measurable by means of wave length $L = 2\pi/\Omega$. The wavy road defined in Eq. (2), initiates vertical vehicle vibrations y described by the equation (1) of motion

$$\ddot{y} + 2D\omega_1(\dot{y} - \dot{z}) + \omega_1^2(y - z) = 0\,, \qquad , \tag{1}$$

$$z(s) = \mathrm{Z}\cos(\Omega s)\,, \qquad s = \mathrm{v}t, \tag{2}$$

where $\omega_1$is the natural frequency of the vehicle and D denotes its damping, given by $\omega_1^2 = c/m$ and $2D\omega_1 = b/m$, respectively. In Eq. (2), Z is the road amplitude and s the longitudinal coordinate $s = \mathrm{v}t$ when the vehicle drives with constant speed v. In the stationary case, Eqs (1) and (2) lead to the amplitude ratio Y/Z of response and excitation

$$(Y/Z\,)^2 = \frac{1+(2D\nu)^2}{(1-\nu^2)^2+(2D\nu)^2}\,, \qquad \nu = \mathrm{v}\,\Omega/\omega_1\,. \tag{3}$$

In Figure 2, the amplitude ratio Y/Z is plotted versus the related frequency speed $\nu = \mathrm{v}\Omega/\omega_1$ for the two damping values $D = 0.1$ and $D = 0.2$. Both curves are drawn in red color. They start in $\nu = 0$ with the ratio $Y/Z = 1$ and end in $\nu = \infty$ with $Y/Z = 0$. They become maximal near the resonance for $\nu = 1$. In Figure 2, λ is the image variable of the vehicle velocity in the range $0 \le \lambda \le 2$ with two different scales: $\lambda = \nu$ in the left half and $\lambda = 2 - 1/\nu$ in the right one. This scaling [6] has the advantage that the amplitude ratio can be drawn for all velocities $0 \le \nu < \infty$.

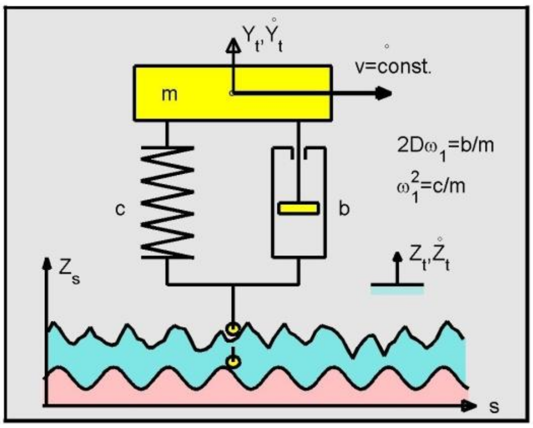

Figure 1: Quarter car model rolling with constant speed v on sinusoidal (orange) or random (cyan) wave roads

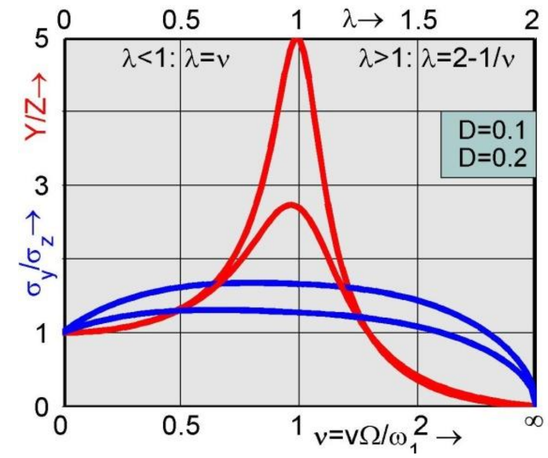

Figure. 2: Standard deviation (blue) and amplitude (red) ratio of response and excitation versus vehicle speed

Stochastic road models [7-12] are assumed to be normally distributed with zero mean and standard deviation σ_z. They are modeled e.g. by means of the linear first order system under white noise

$$dZ_t = -\mathrm{v}\Omega Z_t dt + \sigma\sqrt{\mathrm{v}}dW_t\,, \qquad E(dW_t^2) = dt\,, \tag{4}$$

where $\mathrm{v} > 0$ is the vehicle velocity and σ denotes the intensity of noise realized by the Wiener increment dW_t. The application of the noise spectrum $S_w(\omega) = 1$ and the Fourier transforms leads to the road spectrum

$$S_z(\omega) = \frac{\mathrm{v}\sigma^2}{\omega^2 + (\mathrm{v}\Omega)^2}\,, \qquad \sigma_z^2 = \frac{1}{2\pi}\int_{-\infty}^{+\infty} S_z(\omega)d\omega = \frac{\sigma^2}{2\Omega}\,. \tag{5}$$

The road spectrum is integrated over all frequencies ω to obtain the variance σ_z^2, noted in Eq. (5). The same method can be applied to Eq. (1) to obtain the vehicle spectrum $S_y(\omega)$ which is integrated in order to get the associated standard deviation ratio

$$(\sigma_y/\sigma_z)^2 = \frac{2D+(1+4D^2)\nu}{2D(1+2D\nu+\nu^2)} \quad , \qquad \nu = \mathrm{v}\Omega/\omega_1. \tag{6}$$

In Eq. (6), the time frequency $\mathrm{v}\Omega$ represents the corner frequency of the road spectrum $S_z(\omega)$ in Eq. (5). Now, it takes the role of the middle frequency of the wavy road surface in Eq. (2). In Figure 2, the standard deviation ratio of vehicle response and road excitation, calculated in Eq. (6), is plotted for the same two damping values, as before. Therewith, the result obtained in Eq. (6) can be directly compared with the amplitude ratio in Eq. (3). Obviously, resonance magnifications are much stronger in the harmonic case in comparison with random roads when the vehicle is driving near the resonance velocity $\nu = 1$. Outside of the resonant speed range, however, the magnification is inverted, completely. In the over-critical speed range, the amplification of the standard deviation ratio is more than double as big in comparison with the harmonic case when the vehicle is driving e.g. with $\nu = 2$.

2. Extensions to multiplicative road models

The linear first order road model, determined by the spectrum (5), is extended to multiplicative road models of second order which are introduced by means of the two non-linear stochastic differential (Itô) equations [13, 14]

$$dZ_t = \mathrm{v}\Omega U_t dt, \qquad V_t^2 = 1 - (Z_t/z_0)^2 - (U_t/u_0)^2, \tag{7}$$

$$dU_t = -\mathrm{v}\Omega(2\delta U_t + Z_t)dt + V_t\sigma\sqrt{\mathrm{v}}dW_t\,, \qquad E\left(dW_t^2\right) = dt, \tag{8}$$

where $\mathrm{v} > 0$ denotes the vehicle velocity and σ gives the intensity of white noise dW_t/dt. The parameter Ω is the middle road frequency and δ determines the bandwidth of the two processes Z_t and U_t of the road level and slope, respectively. The non-linear process V_t introduces process limitations by the values z_0 and u_0 which are freely selectable. For infinitely growing values $z_0, u_0 \to \infty$, Eqn. (7) and (8) become linear and their stationary solutions are normally distributed. For finite values $|z_0|, |u_0| < \infty$, the stationary processes are limited by the ellipse $(z/z_0)^2 + (u/u_0)^2 = 1$. In the symmetric case that $z_0 = u_0 = r_0$, the limitation is a circle. When the stationary solutions take vanishing values, multiplicative noise becomes additive with $V_t = 1$ and the system has the strongest possible driving. When the solutions are on the ellipse, noise is excluded by $V_t = 0$ and the system possesses the strongest possible decay behavior.

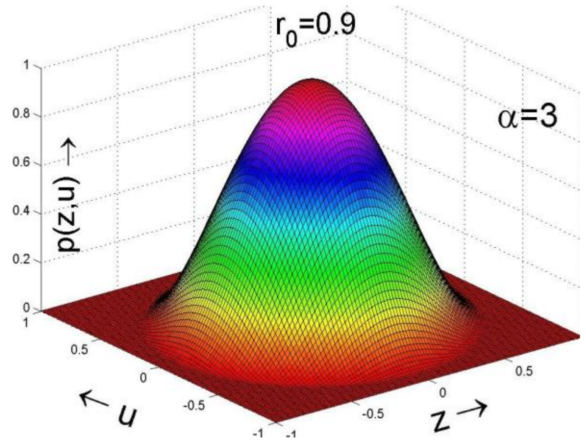

Figure 3: Two-dimensional distribution of level and slope with the limitation $z_0 = u_0 = 0.9$ and the exponent $\alpha = 3$

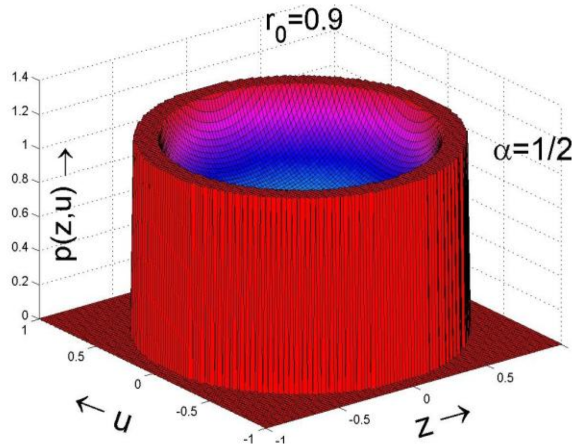

Figure. 4: Singular two-dimensional density of road level and slope for the same limitations and exponent $\alpha = 1/2$

The density distribution $p(z,u,t)$ of the road processes is determined by means of the Fokker-Planck equation [15]

$$\frac{\partial p}{\partial t} = \frac{\partial}{\partial u}[\mathrm{v}\Omega(2\delta u + z)p] - \frac{\partial}{\partial z}[\mathrm{v}\Omega u p] + \frac{1}{2}\sigma^2\mathrm{v}\frac{\partial^2}{\partial \mathrm{u}^2}\left\{\left[1 - \left(\frac{\mathrm{z}}{\mathrm{z}_0}\right)^2 - \left(\frac{\mathrm{u}}{\mathrm{u}_0}\right)^2\right]\mathrm{p}\right\}. \tag{9}$$

In the stationary case, the density $p(z,u)$ is independent on time and satisfies the stationary Fokker-Planck equation

$$0 = 2\delta\left(p + u\frac{\partial p}{\partial u}\right) + z\frac{\partial p}{\partial u} - u\frac{\partial p}{\partial z} + \frac{\sigma^2}{2\Omega}\frac{\partial^2}{\partial u^2}\left\{\left[1 - \left(\frac{\mathrm{z}}{\mathrm{z}_0}\right)^2 - \left(\frac{\mathrm{u}}{\mathrm{u}_0}\right)^2\right]\mathrm{p}\right\}. \tag{10}$$

Note that the velocity v is dropped out in Eq. (10) because of $\partial p/\partial t = 0$; i.e. the statistical configuration of the road is independent on velocity and can be applied for all speeds. In the symmetric case $z_0 = u_0 = r_0$,.Eq. (10) is solved by

$$p(z,u) = C\left[1 - (z/r_0)^2 - (u/r_0)^2\right]^{\alpha-1}, \qquad \alpha = r_0^2 2\delta\Omega/\sigma^2 > 0, \tag{11}$$

where C is the integration constant of normalization. The two-dimensional density, noted in Eq. (11), can be integrated for $\alpha > 0$. This coincides with the stability condition $\delta > 0$ of the linear oscillator for $z_0, u_0 \to \infty$. For $\alpha = 1$, the density $p(z,u)$ in Eq. (11) is uniformly distributed. For $\alpha = 2$, it is parabolic. For $\alpha = 3$, the density $p(z,u)$ possesses a forth order shape as shown in Figure 3 for the limitation $r_0 = 0.9$. In this case, the two-dimensional density is zero on the limitation circle with a vanishing gradient. The two-dimensional density in Eq. (11) becomes singular for $0 < \alpha < 1$. In Figure 4, the density is plotted e.g. for $\alpha = 1/2$. In this case, $p(z, u)$ coincides with the stationary density of the sinusoidal road surface, noted in Eq. (2).

3. Vehicle dynamics with multiplicative road models

The application of Itô's calculus to the multiplicative road model of Eqn. (7) and (8), leads to the three increments

$$d(Z_t^2) = 2\mathrm{v}\Omega Z_t U_t dt, \quad V_t^2 = 1 - (Z_t/z_0)^2 - (U_t/u_0)^2,$$
$$d(Z_t U_t) = \mathrm{v}\Omega(U_t^2 - 2\delta Z_t U_t - Z_t^2)dt + Z_t V_t \sigma\sqrt{\mathrm{v}}\, dW_t,$$
$$d(U_t^2) = -2\mathrm{v}\Omega\left(2\delta U_t^2 + Z_t U_t\right)dt + V_t^2\sigma^2 \mathrm{v}dt + V_t\sigma\sqrt{\mathrm{v}}\, dW_t,$$

in which the expectation operator can be applied to obtain the associated moment's equations. In the stationary case, the first equation and the second one lead to $E(Z_t U_t) = 0$ and $E(U_t^2) = E(Z_t^2)$, respectively. Taking into account that $E(V_t dW_t)$ is vanishing and $E(V_t^2)$ follows from Eq. (7), the third equation gives the stationary square mean

$$E(Z_t^2) = E(U_t^2) = \frac{1}{1/z_0^2 + 1/u_0^2 + 4\delta\Omega/\sigma^2}\,. \tag{12}$$

The result in Eq. (12) coincides with the square means of the linear road model under white noise obtained for the limiting case $z_0, u_0 \to \infty$. Note that the above square mean equations are linear although the state equations (7) and (8) are non-linear. Both is possible because of the specially adapted non-linearity in Eq. (7).

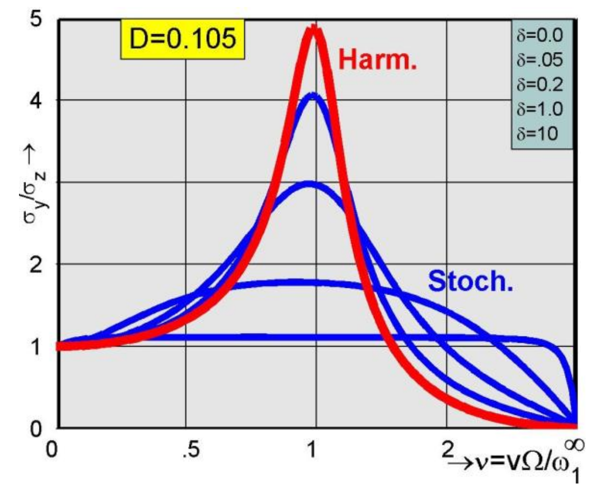

Figure 5: Standard deviation ratio of response and excitation for the road bandwidth $\delta = 0$ (Harm.) and $\delta > 0$ (Stoch.)

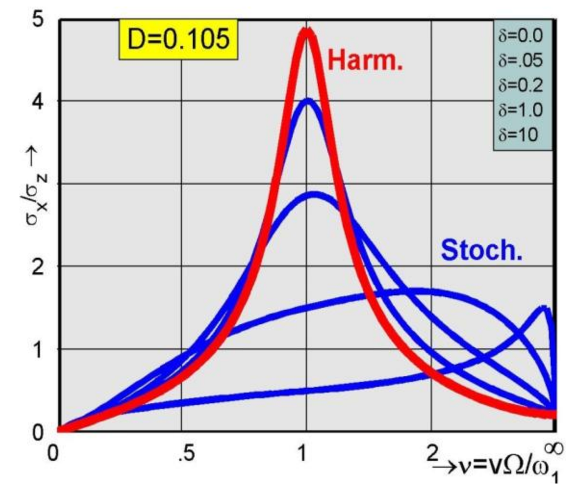

Figure.6: Standard deviation of the vertical vibration velocity versus the related vehicle speed for the damping $D = 0.105$

The multiplicative road model is applied to the quarter vehicle, shown in Figure 1. The introduction of the coordinate $\dot{y} = \omega_1 x$ of the vertical vibration velocity into equation (1) of motion leads to the associated first order system

$$dY_t = \omega_1 X_t dt, \qquad dX_t = -\left[2D\left(\omega_1 X_t - \dot{Z}_t\right) + \omega_1(Y_t - Z_t)\right]dt \tag{13}$$

where the time derivative $\dot{Z}_t$ is given by the increment $dZ_t = \mathrm{v}\Omega U_t dt$ in Eq. (7). The stationary co-variances of all excitation processes Z_t, U_t times all response processes Y_t, X_t are calculable by means of the matrix equation

$$\begin{bmatrix} 0 & -1 & -\nu & 0 \\ 1 & 2D & 0 & -\nu \\ \nu & 0 & 2\delta\nu & -1 \\ 0 & \nu & 1 & 2(D+\delta\nu) \end{bmatrix} \begin{bmatrix} E(Z_t Y_t) \\ E(Z_t X_t) \\ E(U_t Y_t) \\ E(U_t X_t) \end{bmatrix} = \begin{bmatrix} 0 \\ E(Z_t^2) \\ 0 \\ 2D\nu E(U_t^2) \end{bmatrix}, \tag{14}$$

where the square means of the road excitation are already calculated in Eq. (12). Note that the co-variance matrix in Eq. (14) is skew-symmetric. Hence, the co-variance matrix is positive definite. Its determinant Δ is calculated to

$$\Delta = (\nu^2 - 1)^2 + 4\nu(D + \delta\nu)(\delta + D\nu). \tag{15}$$

Subsequently, the stationary moment's equations of the vehicle processes are set up and solved, as follows:

$$E(Y_t^2)/E(Z_t^2) = [1 + 4\nu(D + \delta\nu)(\delta + D\nu) + \delta\nu^3/D\,]/\Delta, \tag{16}$$
$$E(X_1^2)/E(Z_t^2) = \ \nu^2[1 + 4D\nu(\delta + D\nu) + \delta\nu/D]/\Delta\,. \tag{17}$$

In Figure 5 and 6, the square roots of the square mean ratios in Eq. (16) and (17) are plotted versus the related vehicle speed for the damping $D = 0.105$ and five different bandwidth values δ of the road excitation. For vanishing bandwidth $\delta = 0$, the result in Eqn.(16) coincide with the amplitude ratio (3) of a vehicle rolling on wavy roads with harmonic contour surface. The same holds for Eq. (17). For growing bandwidth δ, the resonance peaks in both amplitude-velocity diagrams are reduced in comparison with the harmonic case. However, the standard deviations (blue) become bigger than the amplitude (red) ratios when the vehicle is driving sufficiently outside the resonance velocity. For higher vehicle speeds e.g. $\nu = 2$, the magnification by stochastic excitations becomes even stronger in comparison with the harmonic case. For very slow and very high speeds, the standard deviation ratios are independent on the bandwidth of the road frequencies and coincide with the results of harmonic road excitation. For the special case of white noise with infinitely increasing bandwidth, Eq. (16) gives $\sigma_y/\sigma_z = 1$ for all vehicle speeds $\nu < \infty$ and $\sigma_y/\sigma_z = 0$ for $\nu = \infty$.

4. Non-stationary models of vehicle speed fluctuations

In Figure 1, the wavy road is modeled by the sinusoidal form $z(t)$. This model is extended to its stochastic version

$$Z_t = \cos\phi_t, \qquad d\phi_t = \Omega \mathrm{v} dt + \sigma dW_t, \tag{18a,b}$$

where $\Omega\mathrm{v}$ is the time frequency given by the road frequency Ω times the vehicle velocity v which is perturbed by white noise $\sigma\dot{W}_t$ of intensity σ, when speed fluctuations through driving moment and air resistance are measurable and taken into account in a purely kinematic modeling. The application of Itô's calculus to the road process Z_t leads to

$$dZ_t = -(\Omega \mathrm{v} dt + \sigma dW_t)\sin\phi_t - (\sigma^2/2)\cos\phi_t dt\,.$$

The stochastic road model (18a,b) is applied to Eq. (1) of the vehicle road system in the slightly modified form

$$\ddot{Y}_t + 2D\omega_1\dot{Y}_t + \omega_1^2 Y_t = \mu\left(2D\omega_1\dot{Z}_t + \omega_1^2 Z_t\right), \tag{19}$$

where μ is the amplitude of the road excitation. Note that sinusoidal excitations like $z(t) = \cos\omega t$ are non-stationary with the mean value $m_z = (\omega T)^{-1}\sin\omega T$ which converge to the stationary zero value with linearly growing time T. In order to eliminate this non-stationary behavior, amplitudes A_t, B_t, G_t, H_t are introduced into Eq. (19) by means of Eqn. (20a) and (21a). The application of Itô's calculus leads to the transformed equations, as follows:

$$Y_t = A_t\cos\phi_t + B_t\sin\phi_t\,, \qquad dA_t = (\sigma^2 A_t/2 - \Omega\mathrm{v}B_t + \omega_1 G_t)dt - \sigma B_t dW_t, \tag{20a,b}$$

$$\dot{Y}_t/\omega_1 = G_t\cos\phi_t + H_t\sin\phi_t, \quad dB_t = (\sigma^2 B_t/2 + \Omega\mathrm{v}A_t + \omega_1 H_t)dt + \sigma A_t dW_t, \tag{21a,b}$$

$$dG_t = [-\omega_1 A_t - \Omega\mathrm{v}H_t + (\sigma^2/2 - 2D\omega_1)G_t - \mu(\omega_1 - D\sigma^2)]dt - \sigma H_t dW_t, \tag{22}$$

$$dH_t = [-\omega_1 B_t + \Omega\mathrm{v}G_t + (\sigma^2/2 - 2D\omega_1)H_t - 2D\mu\Omega\mathrm{v}]dt + \sigma(G_t - 2D\mu)dW_t. \tag{23}$$

Numerical integrations of the transformed equations (20b), (21b), (22) and (23) are performed by means of the Maruyana scheme with the time step size $\Delta\tau = \omega_1\Delta t = 10^{-3}$ for $N = 2\cdot 10^7$ samples. The Wiener increments [16] are approximated by $\Delta W_n = N_n\sqrt{\Delta t}$ where the numbers N_n are normally distributed with zero mean and unit mean square $E(N_n^2) = 1$. Associated parameters are chosen by $D = 0.1$, $\mu = 1$ and $\sigma = 0.2\sqrt{\omega_1}$. In Figure 7, simulation results of the displacement means $E(A_t)$ and $E(B_t)$ as well as the density distributions $p(a)$ and $p(b)$ are plotted versus the related speed $\Omega\mathrm{v}/\omega_1$. The density $p(a)$ is marked by blue colour and $p(b)$ is green. Both densities show the resonance effect when the vehicle drives with velocity $\nu = 1$. For further growing speed, the densities of both displacement processes are concentrated around the zero axes. This represents the self-centering effect, already known in rotor dynamics. For $\sigma = 0$, the density distributions $p(a)$ and $p(b)$ degenerate to delta needles around the means values $E(A_t)$ and $E(B_t)$.

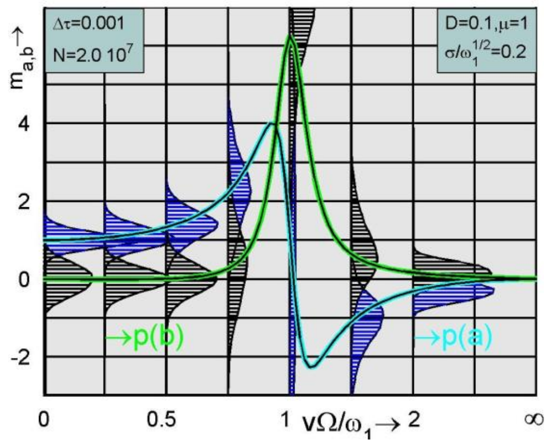

Figure.7: Mean amplitudes and densities of A_t and B_t versus frequency speed related to natural car frequency

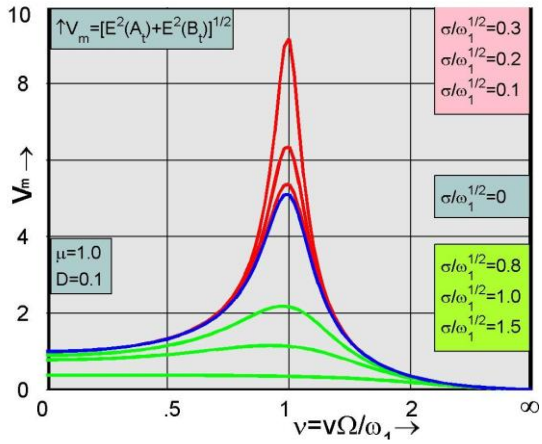

Figure 8: Resonance diagram for growing noise intensity: the resonance is first increased and then decreases again.

The application of the expectation operator $E(\cdot)$ to Eqn. (20b), (21b), (22) and (23) leads to the matrix equation

$$\begin{bmatrix} \sigma^2/2 & -\Omega\mathrm{v} & \omega_1 & 0 \\ \Omega\mathrm{v} & \sigma^2/2 & 0 & \omega_1 \\ -\omega_1 & 0 & \sigma^2/2 - 2D\omega_1 & -\Omega\mathrm{v} \\ 0 & -\omega_1 & \Omega\mathrm{v} & \sigma^2/2 - 2D\omega_1 \end{bmatrix} \begin{bmatrix} E(A_t) \\ E(B_t) \\ E(G_t) \\ E(H_t) \end{bmatrix} = \mu \begin{bmatrix} 0 \\ 0 \\ \omega_1 - D\sigma^2 \\ 2D\Omega\mathrm{v} \end{bmatrix}, \tag{24}$$

by which the stationary mean values of all amplitude processes are calculable. In Figure 8, the resultant mean amplitude $V_m = [E^2(A_t) + E^2(B_t)]^{1/2}$ of both displacement means $E(A_t)$ and $E(B_t)$ is plotted versus the related velocity for vanishing noise (blue) and for growing noise intensity (red). The latter leads to stable mean amplitude with resonance magnifications up to a critical noise intensity where the resonance peak is reduced (green), again. In this case, the mean amplitude mean becomes unstable. This stability behavior follows from the diagonal term $\Delta = (\sigma^2/2 - 2D\omega_1)\,\sigma^2/2$ in Eq. (24) which is negative for weak noise intensities and become positive for growing noise. More details are obtained when the almost sure stability [17] of the amplitudes in Eqs. (20b), (21b). (22) and (23) is investigated. Stability in mean is investigated by means of the eigen-values [17] of the mean amplitudes matrix in Eq. (24).

5. Resonance reduction and induction by means of filtered noise

It is interesting how the resonance behavior of the amplitude processes is changing when the velocity perturbation by white noise $\sigma\dot{W}_t$ in Eq. (18b) is replaced by the more realistic perturbation of filtered noise $\omega_g\Psi_t$, as follows:

$$\dot{Y}_t = \omega_1 X_t\,, \qquad \dot{\Phi}_t = \Omega\mathrm{v} + \omega_g\Psi_t\,, \quad d\Psi_t = -\omega_g\Psi_t dt + \sigma dW_t, \qquad (25\,a,b,c)$$

$$\dot{X}_t = -\omega_1(2DX_t + Y_t) + \mu[\omega_1\cos\Phi_t - 2D(\Omega\mathrm{v} + \omega_g\Psi_t)\sin\Phi_t]. \qquad (26)$$

The stationary filtered noise in Eq. (25c) is normally distributed with zero mean and mean square $\sigma_\psi^2 = \sigma^2/(2\omega_g)$. The application of the amplitude processes (20a) and (21a) to the vehicle equations (25a) and (26) leads to

$$d\vec{V}_t = (A\vec{V}_t + \omega_g B\Psi_t\vec{V}_t)dt + \mu(\vec{x} - 2D\omega_g\Psi_t\vec{y})dt, \qquad (26)$$

where the vector $\vec{V}_t = (A_t, B_t, G_t, H_t)'$ of the four amplitudes are determined by the matrices A and B as follows:

$$A = \begin{bmatrix} 0 & -\Omega\mathrm{v} & \omega_1 & 0 \\ \Omega\mathrm{v} & 0 & 0 & \omega_1 \\ -\omega_1 & 0 & -2D\omega_1 & -\Omega\mathrm{v} \\ 0 & -\omega_1 & \Omega\mathrm{v} & -2D\omega_1 \end{bmatrix}, \qquad B = \begin{bmatrix} 0 & -1 & 0 & 0 \\ 1 & 0 & 0 & 0 \\ 0 & 0 & 0 & -1 \\ 0 & 0 & 1 & 0 \end{bmatrix}$$

$$\vec{V}_t = (A_t, B_t, G_t, H_t)', \qquad \vec{x} = (0,0,\omega_1,-2D\Omega\mathrm{v})', \qquad \vec{\mathrm{y}} = (0,0,0,1)'.$$

The vectors $\vec{x}$ and $\vec{y}$, noted above, determine the inhomogeneous part in Eq. (26). Note that in Eq. (26) there is a non-linear term in form of $\Psi_t\vec{V}_t$ with a product of state processes. The product possesses the increment

$$d(\Psi_t\vec{V}_t) = [A\Psi_t\vec{V}_t + \omega_g B\Psi_t^2\vec{V}_t + \mu(\Psi_t\vec{x} - 2D\omega_g\Psi_t^2\vec{y}) - \omega_g\Psi_t\vec{V}_t]dt + \vec{V}_t\sigma dW_t, \qquad (27)$$

which couples the system vector $\vec{V}_t$ to higher potencies of the perturbation Ψ_t. This coupling effect is approximately removed in the stationary moments equations of Eqn. (26, 27) by means of the Gaussian closure, as follows:

$$AE(\vec{V}_t) + \omega_g BE(\Psi_t\vec{V}_t) = -\mu\vec{x}\,, \qquad E(\Psi_t^2\vec{V}_t) = E(\Psi_t^2)E(\vec{V}_t), \qquad (28a,b)$$

$$\omega_g\sigma_\psi^2 BE(\vec{V}_t) + (A - \omega_g I)E(\Psi_t\vec{V}_t) = \mu 2D\omega_g\sigma_\psi^2\,\vec{y}\,, \qquad E(\Psi_t^2) = \sigma^2/(2\omega_g). \qquad (29a,b)$$

In Eq. (29a), I denotes the unit matrix. Note that in Eq. (29a) the expectation of the product $\Psi_t^2\vec{V}_t$ is approximately replaced by the product of both mean values. Numerical evaluations of Eqn. (28a) and (29a) are shown in Figure 9 where the mean amplitude V_m is plotted versus the vehicle velocity ν for $D = 0.1$, $\mu = 1$ and the noise intensities $\sigma = 0.2\sqrt{\omega_1}$ (green) and $\sigma = 0.5$ (blue). For $\omega_g = 0$, the green and blue lines coincide with the deterministic case of vanishing perturbations. For growing bandwidth of the perturbation, the resonance peak is reduced. The resonance reduction becomes stronger for increasing noise intensities σ and for increasing low-pass frequency ω_g. This effect is physically explainable by the fact that high frequencies are filtered out and only low frequencies are retained in the perturbation. However, low velocity frequencies $\mathrm{v}\Omega$ are not contributing to resonance effects.

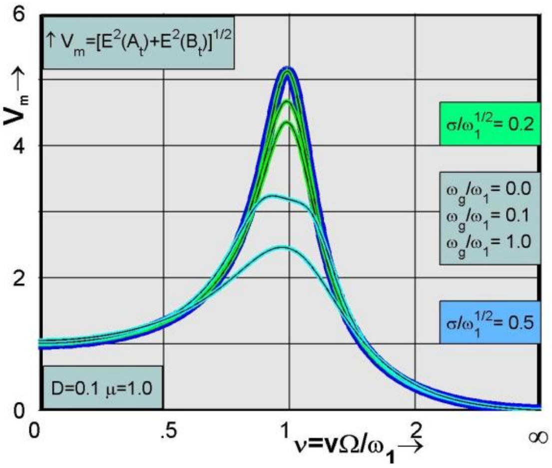

Figure.9: Resonance reduction in the mean amplitudes V_m for growing noise intensity and perturbation bandwidth

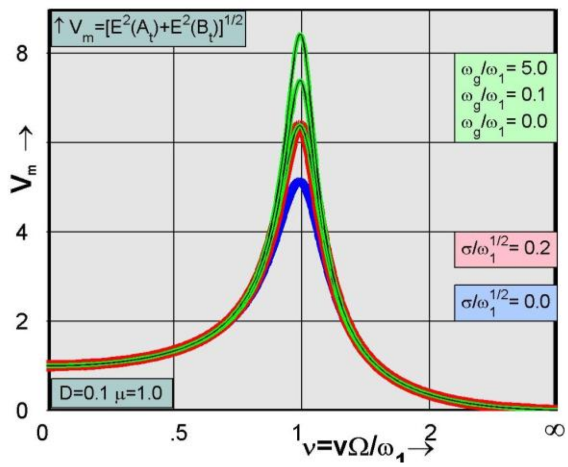

Figure 10: Resonance induction from blue to red line via growing noise intensity and perturbation bandwidth (green)

The resonance reduction is completely inverted when instead of low-pass noise one applies the high-pass perturbation

$$Z_t = \cos\phi_t, \qquad \dot{\Phi}_t = \Omega\mathrm{v} + \dot{\Psi}_t\,, \quad d\Psi_t = -\omega_g\Psi_t dt + \sigma dW_t, \qquad (30abc)$$

where white noise $\sigma\dot{W}_t$ in Eq. (18b) is now replaced by $\dot{\Psi}_t$ in Eq. (30b). Consequently, perturbations with low frequencies are filtered out. High frequency parts are retained. The introduction of Eqn. (30) into Eq. (19) leads to

$$dY_t = \omega_1 X_t dt, \qquad d\phi_t = (\Omega v - \omega_g\Psi_t)dt + \sigma dW_t\,, \quad d\Psi_t = -\omega_g\Psi_t dt + \sigma dW_t, \quad (31a,b,c)$$

$$dX_t = -\omega_1(2DX_t + Y_t)dt + \mu\big[(\omega_1 - D\sigma^2)\cos\phi_t + (\omega_g\Psi_t - \Omega\mathrm{v})\sin\phi_t\big]dt - \mu 2D\sigma\sin\phi_t dW_t\,. \qquad (32)$$

The application of the amplitude processes (20a) and (21a) to Eqn. (31) and (32) leads to the vector equation

$$d\vec{V}_t = \big(A\vec{V}_t - \omega_g B\Psi_t\vec{V}_t\big)dt + \mu\big(\vec{x} + 2D\omega_g\Psi_t\vec{y}\big)dt + \big(B\vec{V} - 2D\mu\vec{y}\big)\sigma dW_t \qquad (33)$$

where the vector $\vec{V}_t$ contains the four amplitude processes. The matrix A and the vectors $\vec{x}$ are given by

$$A = \begin{bmatrix} \sigma^2/2 & -\Omega\mathrm{v} & \omega_1 & 0 \\ \Omega\mathrm{v} & \sigma^2/2 & 0 & \omega_1 \\ -\omega_1 & 0 & \sigma^2/2 - 2D\omega_1 & -\Omega\mathrm{v} \\ 0 & -\omega_1 & \Omega\mathrm{v} & \sigma^2/2 - 2D\omega_1 \end{bmatrix}, \qquad \vec{x} = \begin{bmatrix} 0 \\ 0 \\ \omega_1 - 2D\,\sigma^2/2 \\ -2D\Omega\mathrm{v} \end{bmatrix}, \qquad .$$

where B and $\vec{y}$ are already noted in the last section. The non-linear term $\Psi_t\vec{V}_t$ in Eq. (33) possesses the increment

$$d(\Psi_t\vec{V}_t) = \big[A\Psi_t\vec{V}_t + \omega_g B\Psi_t^2\vec{V}_t + \mu(\Psi_t\vec{x} - 2D\omega_g\Psi_t^2\vec{y}) - \omega_g\Psi_t\vec{V}_t\big]dt + \vec{V}_t\sigma dW_t \qquad (34)$$

in which the system vector $\vec{V}_t$ is coupled to higher potencies of the perturbation Ψ_t. This coupling is approximately removed by means of the Gaussian closure, noted in Eq. (35b). In the stationary case, the insertion of the Gaussian closure condition into Eq. (34) leads to the linear moments equations

$$AE(\vec{V}_t) - \omega_g BE(\Psi_t\vec{V}_t) = -\mu\vec{x}\,, \qquad E(\Psi_t^2\vec{V}_t) = E(\Psi_t^2)E(\vec{V}_t), \qquad (35a,b)$$

$$BE(\vec{V}_t)\sigma^2/2 + (A - \omega_g I)E(\Psi_t\vec{V}_t) = \mu 2D\vec{y}\sigma^2/2\,, \qquad E(\Psi_t^2) = \sigma^2/(2\omega_g). \qquad (36a,b)$$

where I is the unit matrix. Numerical evaluations of Eqs. (35a) and (36a) are shown in Figure 10 where the mean amplitude V_m is plotted versus the related vehicle velocity v for $D = 0.1$ and $\mu = 1.$ The blue line stands for $\sigma = 0$ of vanishing noise perturbations. For $\sigma = 0.5\sqrt{\omega_1}$ and $\omega_g/\omega_1 = 0,$ one obtains the red line overlaid by the green one in coincidence with the white noise case shown in Figure 8. For $\omega_g/\omega_1 = 0.1$ and $\omega_g/\omega_1 = 5$ of growing perturbation bandwidth, there is a further increasing of the resonance peak. This resonance induction is probably explained by the destabilizing effect of harmonic parameter excitations when for $\Omega\mathrm{v} = 2\omega_1$ the perturbation frequency coincides with the double eigen-frequency of the oscillator.

6. Lyapunov exponents and rotation numbers in vehicle dynamics

Vehicle vibrations which are described by rotating coordinates are physically existent if they are almost sure stable or asymptotically stable with probability one. In the unstable case, the separation into rotating processes is not possible and the vehicle equations must be retransformed back to their original equations in non-rotating coordinates. The stability in mean and the almost sure stability [17] of the vehicle vibrations in rotating coordinates is investigated by means of a projection on hyper-spheres and application of the multiplicative ergodic theorem of Osceledets [18]. For these purposes, Eqn. (20b), (21b), (22) and (23) are reduced with $\mu = 0$ to the homogenous form and transformed by means of the two-dimensional system of polar coordinates (P_t, Γ_t) and (Q_t, θ_t), which leads to the stability equations

$$A_t = P_t\cos\Gamma_t: \qquad dP_t = [\omega_1\cos(\Theta_t - \Gamma_t)\,Q_t + \sigma^2 P_t]dt,$$

$$B_t = P_t\sin\Gamma_t: \qquad d\Gamma_t = [\omega_1\sin(\Theta_t - \Gamma_t)\tfrac{Q_t}{P_t} + \Omega\mathrm{v}]dt + \sigma dW_t,$$

$$G_t = Q_t\cos\Theta_t: \qquad dQ_t = [-\omega_1\cos(\Theta_t - \Gamma_t)\,P_t + (\sigma^2 - 2D\omega_1)Q_t]dt,$$

$$H_t = Q_t\sin\Theta_t: \qquad d\Theta_t = [\omega_1\sin(\Theta_t - \Gamma_t)\tfrac{P_t}{Q_t} + \Omega\mathrm{v}]dt + \sigma dW_t.$$

The above equations project the displacements (A_t, B_t) and the velocities (G_t, H_t) on two circles with radii (P_t, Q_t) and angles (Γ_t, Θ_t). A second application of polar coordinates by means of Eqs. (37a) and (38a) eliminates the two radii (P_t, Q_t) and projects the entire motion on hyper-sphere with one radius R_t and three angles determined by

$$P_t = R_t\cos\Psi_t: \qquad dR_t = [\sigma^2 - D\omega_1(1 - \cos 2\Psi_t)]R_t dt, \qquad (37)$$

$$Q_t = R_t\sin\Psi_t: \qquad d\Psi_t = -\omega_1(D\sin 2\Psi_t + \cos\Delta_t)dt, \qquad (38)$$

$$\Delta_t = \theta_t - \Gamma_t: \qquad d\Delta_t = \omega_1\sin\Delta_t(\cot\Psi_t - \tan\Psi_t)dt, \qquad (39)$$

$$\Sigma_t = \theta_t + \Gamma_t: \qquad d\Sigma_t = \omega_1\sin\Delta_t(\cot\Psi_t + \tan\Psi_t)dt + 2\omega_e dt + 2\sigma dW_t, \qquad (40)$$

where difference and sum angle (Δ_t, Σ_t) are additionally introduced by means of Eqn. (39a) and (40a). Eq. (37) is integrated by means of variable separation and leads to the top Lyapunov exponent

$$\lambda_{top} = \lim_{t\to\infty}\frac{1}{t}\ln(R_t/R_0) = \sigma^2 - D\omega_1\left(1 - \lim_{t\to\infty}\frac{1}{t}\int_0^t \cos 2\Psi_\tau d\tau\right). \qquad (41)$$

If the top Lyapunov exponent is negative, the stationary solutions of Eqn. (20b), (21b), (22) and (23) are asymptotically stable with probability one or almost surely stable. For $\lambda_{top} > 0$, the solutions are unstable and grow, exponentially.

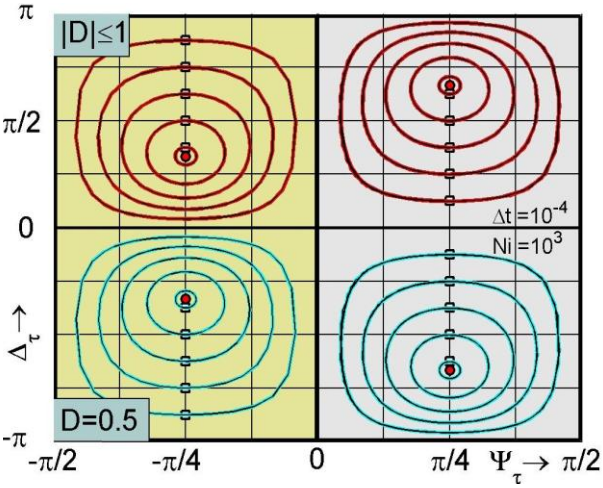

Fig. 11: Limit cycles of projection angles Δ_τ and Ψ_t around red centers for under-critical damping $D \leq 1$

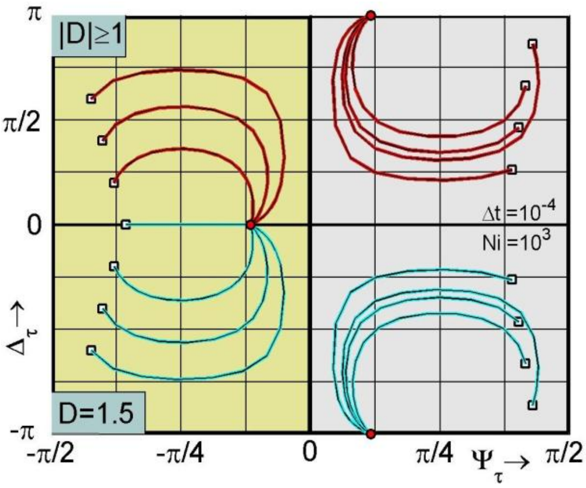

Fig. 12: Transient projection angles and their ending in singular fix-points for over-critical damping $D \geq 1$

According to Eq. (41), the top Lyapunov exponent is determined by the noise intensity, the system damping and the time average of the cosine of the stability angle Ψ_t, which is coupled with the difference angle Δ_t. Both angles are determined by Eqn. (38b) and (39b) which are non-linear, noise-free and decoupled from the sum angle Σ_t in Eq.(40b) where additive noise is still active. In Figure 11 and 12, Eqn. (38b) and (39b) are numerically evaluated for the under- and overcritical damping $D = 0.5$ and $D = 1.5$ on the left and right side, respectively. The angle solutions are 2π −periodic in Δ and π −periodic with respect to Ψ. For $D \leq 1$, Figure 11 shows stationary limit cycles of both angles $(\Lambda_\tau, \Psi_\tau)$. They are calculable without any transient time behavior for arbitrary initial values applying an Euler scheme e.g. with the scan rate $\Delta_\tau = \omega_1 \Delta t = 0.001$. All limit cycles in Figure 11 are symmetric with respect to $\Psi = \pm\pi/4$. Because of this symmetry the time average in Eq. (41) can also be obtained by the four stationary fix-points $\Psi = \pm\pi/4$ and $\cos\Delta = \pm D$ which represent the center of the limit cycles marked by red circles. The insertion of these center values into Eq. (41) leads to one top Lyapunov exponent and two rotation numbers, as follows:

$$\lambda_{top} = \sigma^2 - D\omega_1 \quad \text{and} \quad \rho_{\Gamma,\theta} = \Omega \text{v} \pm \omega_1\sqrt{1-D^2} \qquad \text{for } D \leq 1. \tag{42}$$

The rotation numbers are time averages of rotating angle processes, applied to the angles increments $d\Gamma_t$ and $d\Theta_t$. They are calculated by the stationary values $(\sin\Delta)^2 = 1 - D^2$ and $Q/P = \tan\Psi = \pm 1$. In Figure 12, Eqn. (38b) and (39b) are evaluated for the overcritical damping $D = 1.5$ where instead of limit cycles transient solutions are obtained. Starting with any initial values, both angles $(\Lambda_\tau, \Psi_\tau)$ move to the stationary fix-points $\Delta = 0, \pm\pi$ and $\sin 2\Psi = \pm 1/D$. The insertion of these stationary angle values leads to two Lyapunov exponents and one rotation number

$$\lambda_{1,2} = \sigma^2 - \omega_1\left(D \mp \sqrt{D^2-1}\right) \quad \text{and} \quad \rho_{\Gamma,\theta} = \Omega\text{v} \qquad \text{for } D \geq 1. \tag{43}$$

where the fix-points solutions are inserted into the ergodic integrals of Lyapunov exponent and rotation number.

In Figure 13, the rotation numbers are plotted versus the frequency speed Ωv for the natural frequency $\omega_1 = 1$ and three damping values. For $D = 0$, one obtains two straight lines with positive slopes marked by thick red color. For $D = 0.9$, both rotation numbers are drawn in green and coincide in yellow for $D = 1$. Associated rotation numbers with negative slopes are obtained for negative speed frequencies. In Figure 14, the stability map is obtained by plotting the related critical noise intensity σ_{cr}^2/ω_1 versus the vehicle damping. With $\lambda_{top} = 0$, the stability boundaries are

$$\sigma_{cr}^2/\omega_1 = D \qquad \text{for} \quad D \leq 1,$$
$$\sigma_{cr}^2/\omega_1 = D - \sqrt{D^2-1} \qquad \text{for} \quad D \geq 1.$$

In Figure 14, the stability region is marked by green color. Inside the green region, the stationary solutions of Eqn. (20b), (21b), (22) and (23) are asymptotically stable with probability one or almost surely stable. Over the green region, the solutions are unstable. Obviously, one needs linearly increasing to stabilize the system for growing noise. However, this effect holds up to $D = 1$, only. Overcritical damping is less effective since growing damping stabilizes weak noise perturbations, only. For $D \to \infty$, vehicle and road are rigidly coupled. Hence, stabilization is no longer possible. For an extended stability investigation, the above polar coordinate system (P_t, Γ_t) and (Q_t, θ_t) is applied to Eq.(24). For $\mu = 0$, this leads to the same stability equations for the angles (Γ_t, θ_t) and radii (P_t, Q_t) except that σ^2 in the radii equations is replaced by $\sigma^2/2$ when because of $E(dW_t) = 0$ there is noise in Eq. (24). Therewith, the radius equation (37) reads as

$$dR_t = [\sigma^2/2 - D\omega_1(1 - \cos 2\Psi_t)]R_t dt. \tag{44}$$

As already shown before, the Lypaunov exponents of the mean value solutions are calculated to

$$\lambda_{m,} = \sigma^2/2 - D\omega_1, \qquad \text{for} \qquad D \leq 1,$$
$$\lambda_{m,} = \sigma^2/2^2 - \omega_1\left(D \mp \sqrt{D^2-1}\right), \qquad \text{for} \qquad \text{for } D \geq 1.$$

The rotation numbers of the mean value solutions remain unchanged. In Figure 12, the stability boundaries of the mean value solutions are plotted in Figure 14, marked by blue lines. Note that stability and rotation behavior of the mean value solutions can also investigated by means of the four eigen-values of Eq. (24) where the real and imaginary parts take the role of Lyapunov exponents and rotation numbers, respectively. Correspondingly, one finds one real part and four imaginary parts for $D \leq 1$. In the overcritical case $D \geq 1$, the eigen-values of Eq. (24) lead to two real parts and two imaginary parts. According to [19], the stability behavior can also be investigated by means of the p-th mean behavior in order to get the almost sure stability for $p = 0$ and the stability in mean for $p = 1$. In [21], one finds approximations of stability boundaries of second order systems for all exponents $p \geq 0$.

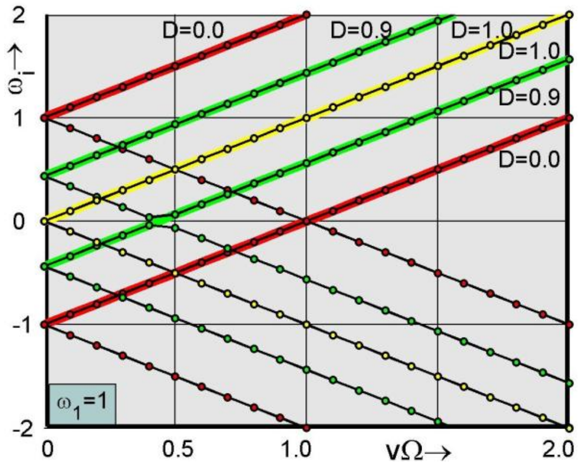

Fig. 13: Four rotation numbers depending on speed frequency for the damping values $D = 0, 0.9$ and 1.0

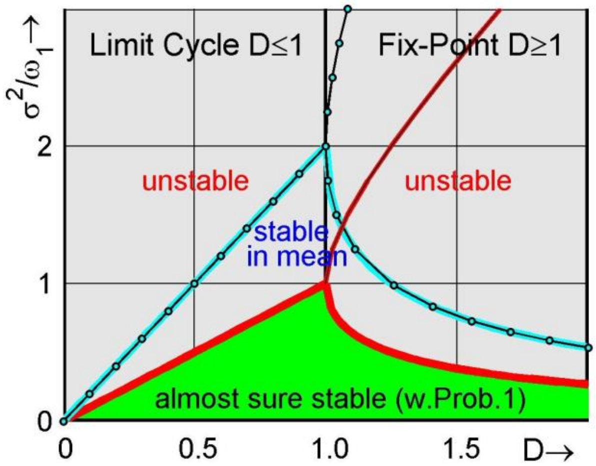

Fig. 14: Boundaries for almost sure stability and stability in mean plotted against system damping

7. Conclusions

There are two multiplicative road models which include the limiting case of deterministic harmonic roads. The first one is obtained by non-linear filter equations driven by white noise. Their stationary solutions are similar to Gaussian but bounded with vanishing mean and standard deviation which coincides with the deterministic behavior in the limiting case of vanishing excitation bandwidth $\delta = 0$. Because of specially adapted non-linearity, the mean square equations calculated by means of Itô's calculus are linear. The second model applies sinusoidals where the excitation frequency is perturbed by white noise of intensity σ. Inversely to the first model, standard deviations are zero and mean values coincide with the deterministic harmonic behavior passing to the limit case $\sigma = 0$ of vanishing noise perturbation. New results are found for more realistic perturbations by means of filtered noise. For low-pass filtered perturbations, the resonance peak is reduced. However, it is increased applying white noise perturbations. This resonance induction is even stronger when instead of white noise high-pass filtered perturbations are applied.

References

[1] Wedig, W.V.: Dynamics of Cars Driving on Stochastic Roads, In: Spanos & Deodatis (Eds), Rotterdam, Millpress, 647-654, 2003.
[2] Wedig, W.V.: Digital Simulation of Road-Vehicle Systems. Prob. Engineering Mechanics, 27, pp. 82-87. 2012.
[3] Wedig, W V.: Velocity Turbulences in Stochastic Road-Vehicle Dynamics, Proc. of the 15th Intern. Prob. Workshop, Dresden 2017, TUDpress, 1-13.
[4] Popp, K. and Schiehlen, W.O.: Fahrdynamik, Teubner, 1993.
[5] Rill,G.: Road Vehicle Dynamics: Fundamentals and Modeling, CRC Press, Boca Raton FL, 2012.
[6] Klotter, K.: Kinetik der Schwinger, Hütte, Theoretische Grundlagen, 4. Abschnitt Schwingungen, w. Ernst & Sohn, Berlin, 571-584, 1955
[7] Doods, C.J. and Robson, D.J.: The Description of Road Surface Roughness, Journal Sound and Vibration, 31, 175-183, 1973
[8] Sobczyk, K., MacVean, D.B. and Robson, J.D. :Response to Profile-Imposed Excitation with Randomly Varying Transversal Velocity, Journal . . Sound and Vibration, 52, 1, pp. 37-49, 1977.
[9] Braun, O. Untersuchungen von Fahrbahnunebenheiten und Anwendungen der Ergebnisse, Diss. Universität Hannover,1969.
[10] Wedig, W.V.: Simulation of Road-Vehicle Systems, Probabilistic Engineering Mechanics, 27, 82-87, 2012.
[11] Wedig, W.V. Jump Phenomena in Road-Vehicle Dynamics, Int. Journal of Dynamics and Control, 4, 21-28, 2016
[12] Wedig, W.V. New Resonances and Velocity Jumps in Nonlinear Road-Vehicle Dynamics, in: Proceedings of IUTAM Symposium on Analytical . Methods in Nonlinear Dynamics, P. Hagedorn (ed.), 2015, Procedia IUTAM, Elsevier, 1-9. 2016 (available online at www.sciencedirect.com).
[13] Arnold, L.: Stochastic Differential Equations. New York, Wiley, 1974.
[14] Itô, K.: On stochastic differential equations, American Math. Society 4, 1-51, 1951.
[15] Bunke, H.: Gewöhnliche Differentialgleichungen mit zufälligen Parametern, Akademie, Berlin, 1972.
[16] Kloeden, P. and Platen, P E.: Numerical Solution of Stochastic Differential Equations: A Review, Heidelberg, Springer, 1995.
[17] Wedig, W.V.: Lyapunov Exponents and Rotation Numbers in Rotor and Vehicle Dynamics, Procedia Engineering, 199, 875-881, 2017.
[18] Oseledets. V. I. :A multiplicative ergodic theorem: Lyapunov characteristic numbers for dynamical systems. Trans. Moscow Math. Soc. 19, (1968), 197–231.
[19] Arnold, L.: Random dynamical systems. Springer Verlag, 2003.
[20] Wedig, W.V.: Lyapunov exponent of stochastic systems and related bifurcation problems. In:Stochastic Structural Dynamics–Progress in Theo . Theory and Applications, eds. Ariaratnam, Schueller, & Elishakoff, Elsevier Applied Science, 315-327, 1988.